SOME OBSERVATIONS ON ARTIFICIAL BULK VISCOSITY IN LS-DYNA: WHAT NOH KNEW IN 1978

Len Schwer

July 2015

Abstract

A review of the development background for artificial bulk viscosity is presented with a focus on the development implemented in LS-DYNA and similar to other explicit codes. The analytical solution and benchmark calculation results presented by Noh (1978) for a one dimension shock problem are used to indicate errors in the simulation results attributed by Noh to artificial bulk viscosity. Noh identifies and demonstrates three types of artificial bulk viscosity errors: (1) excess shock heating, (2) non-uniform meshing and (3) due to spherical geometries. The LS-DYNA Multi-Material ALE solver is used to model Noh's shock problem and the results are reported for plane strain, axisymmetric (cylindrical) and spherical geometries; the latter being of practical importance in modeling free air bursts.

Several appendices are include that cover closely related topics: the role of bulk viscosity in time step stability calculations, solution of the Rankine–Hugoniot Jump Conditions for Noh's plane strain case, and a comparison of four explicit solver results for the spherical geometry case.

Introduction

Perhaps the most lucid discussion of shock viscosity, a.k.a. artificial bulk viscosity, is Section 2.8 "The shock viscosity in one dimension" in the paper by Benson (1992), from which this manuscript borrows, in part. Calculations involving shocks have long used the numerical artifice of shock viscosity to obtain reasonable solutions in a numerical continuum mechanics framework for the discontinuities associated with shocks. The role of the shock viscosity is to spread out the shock thickness (discontinuity) over several elements. Thus the mesh refinement must be fine enough to allow for this approximation.

Strong shocks in gases are dissipative due to both the gas heating caused by the large and rapid compression of the gas and viscosity among the gas molecules in the densified shock thickness. Most numerical shock viscosity algorithms lump these two dissipative mechanisms together and treat the resulting viscosity as a pressure term.

Von Neumann and Richtmyer (1950) introduced a pressure viscosity term in their work with one dimensional shock propagation

$$q = -\rho\left(c\Delta x\right)^2 \frac{\partial u}{\partial x}\left|\frac{\partial u}{\partial x}\right| \tag{1}$$

where ρ is the density, c is a dimensionless constant to be selected, Δx is the mesh spacing and u is the velocity. This viscosity is positive for compressive strain rates, i.e. $\partial u / \partial x < 0$, and negative for rarefactions. Typically, numerical implementations of such shock viscosities only activate the term for compressive strain rates, LS-DYNA use this implementation.

The one dimensional viscosity of Von Neumann and Richtmyer is both effective and deceptively simple. In one dimension the strain rate across the shock, and hence velocity jump, is easily determined:

$$\Delta u = \Delta x \frac{\partial u}{\partial x} \tag{2}$$

In expanding this concept to two or three dimensions, the determination of the direction for calculating the strain rate across the shock becomes more challenging. The simplest approximation is to replace the element length by the square root of the element area in two dimensions, or the cube root of the volume in three dimensions. The strain rate across the shock is approximated as the trace of the strain rate tensor, i.e.

$$\frac{\partial u}{\partial x} \approx \dot{\varepsilon}_{kk} \tag{3}$$

The standard form of the shock viscosity used in many explicit codes today is a combination of the quadratic term proposed by Von Neumann and Richtmyer for strong shocks and a linear term for treating small oscillations that occur after the shock:

$$q = \rho l\left(Q_1 l \dot{\varepsilon}_{kk}^2 - Q_2 a \dot{\varepsilon}_{kk}\right) \tag{4}$$

This is the form used by LS-DYNA for compressive strain rates where l is the generalize length parameter mentioned above, a is the local sound speed, and Q_1 & Q_2 are dimensionless constants, by default in LS-DYNA set to 1.5 and 0.06, respectively.

Artificial Bulk Viscosity Induced Errors

In an exhaustive study of shock viscosity associated errors, Noh (1978) includes a verification problem run in one, two and three dimensions corresponding to the geometries for plane strain, cylindrical (axisymmetric) and spherical problems. The problem is similar to Sod's Problem for

a one dimensional shock tube or a one dimensional piston driven shock. A one dimensional domain of length unity with an ideal gas $(\gamma = 5/3)$ is fixed at the left end $R(0,t) = 0$ and has a prescribed velocity of unity at the other end $u(1,t) = -1$; negative velocity pointing towards the origin. All points in between these ends have the following initial conditions: velocity toward the origin $u(r,0) = u^0 = -1$, initial density $\rho(r,0) = \rho^0 = 1$, initial internal energy $\varepsilon = (r,0) = \varepsilon^0 = 0$ and initial pressure $p^0 = (\gamma - 1)\rho^0\varepsilon^0 = 0$.

Figure 1 through Figure 3 show the analytical solutions for the three geometries at time t=0.6. Since the shock speed is 1/3, i.e. $S = u^0(\gamma - 1)/2$, the shock front is located at $R = St = 0.6/3 = 0.2$. The general solution for the density ahead of the shock is $\rho = \rho^0(1 + t/R)^{\delta - 1}$ where $\delta = 1,\ 2,\ 3$ for the three geometric dimensions. The increasing density for $\delta = 2$ & 3, i.e. axisymmetric and spherical geometries, is due to the converging geometry as material flows towards the origin. The plane strain analytical solution of the Rankine–Hugoniot Jump Conditions is presented in an appendix.

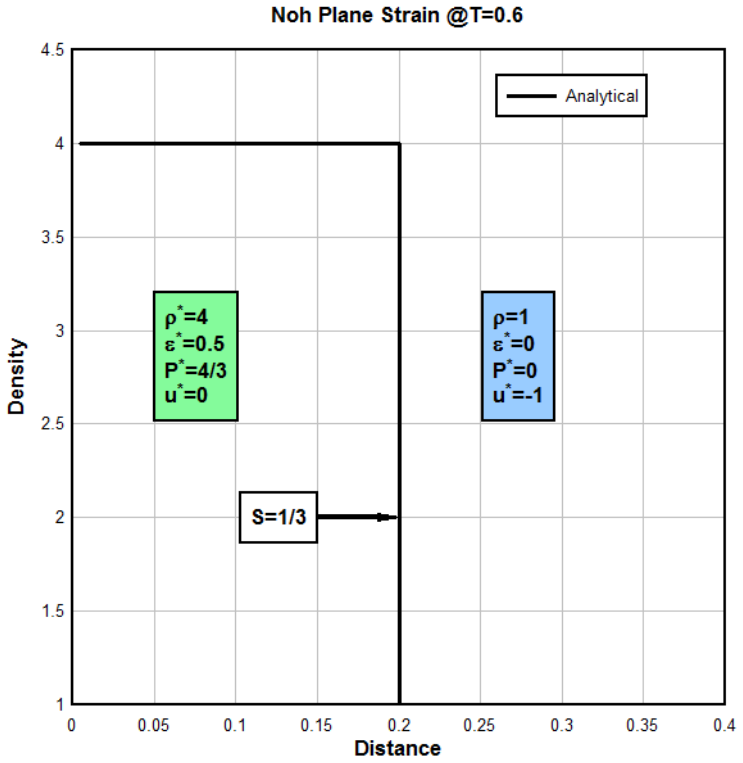

Figure 1 Analytical solution for Noh's verification problem in one dimension plane strain.

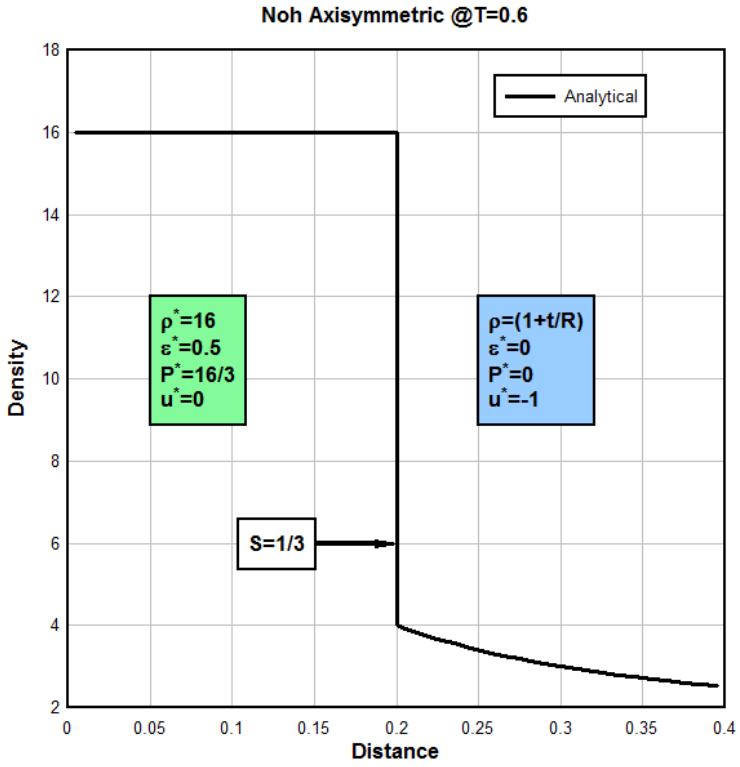

Figure 2 Analytical solution for Noh's verification problem in two dimensions cylindrical.

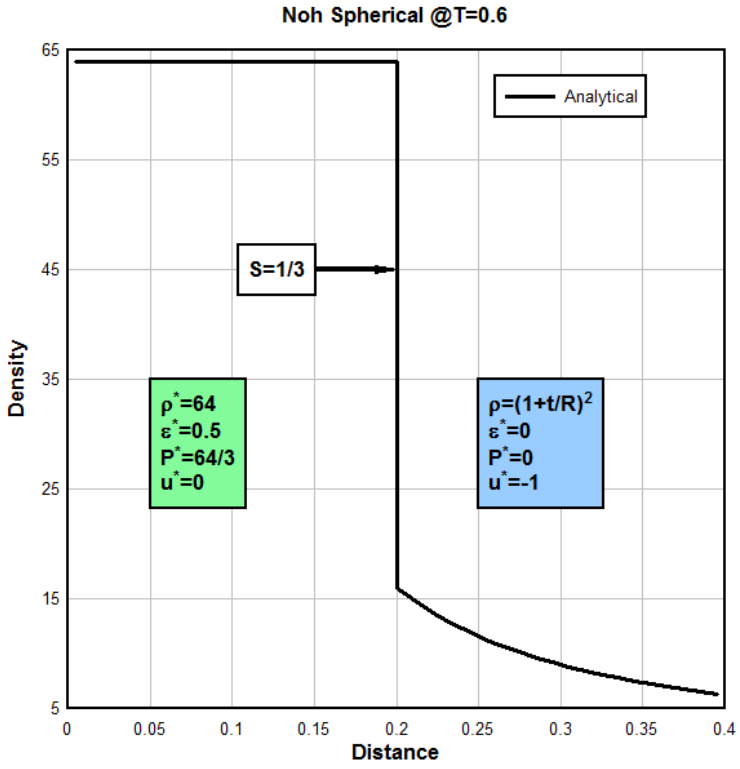

Figure 3 Analytical solution for Noh's verification problem in three dimensions spherical.

Simulation Results

The unit length ideal gas domain is discretized using uniform beam elements of lengths: 0.02, 0.01, 0.005, 0.00125 and 0.0006, with 0.01 being the nominal mesh size used by Noh Note: Noh's finest discretization was 0.00125 for the spherical geometry, but as will be shown, the results are not converged, so an additional mesh refinement of 0.0006 was included. The LS-DYNA mesh was modified such that the most distant beam element was a different ALE Multi-Material Group, but with the same ideal gas properties and initial conditions; two[1] AMMGs are needed for MM-ALE using ALEFORM=11. Subsequently, the only model change required in going from one geometric dimension to another was changing the element formulation: ELFORM=7 for plane strain, =8 for axisymmetric and =-8 (minus 8) for spherical geometries.

Unless otherwise stated, the artificial bulk viscosity coefficients were $Q_1 = 1.5$ and $Q_2 = 0.06$ the LS-DYNA defaults. Also, the hourglass form used was IHQ=2 (viscous – internally changed from =3 input) with the default coefficient QM=0.1. Note: since the initial density of this ideal gas is $\rho = 1$, the hourglass coefficient was not internally reduced by LS-DYNA as is typically done for gases. *MAT_NULL was combined with *EOS_LINEAR_POLYNOMIAL setting $C_4 = C_5 = \gamma - 1$ and $E_0 = 0$ to model the initially cold ideal gas.

Tracer particles were located ever 0.005 along the first 0.3 or 0.4 length of the ideal gas domain. Histories of density, also pressure and velocity, were sampled at these locations at t=0.6 to allow comparison with the plots presented by Noh.

One Dimensional Plane Strain Simulation Results

Figure 4 shows comparisons of the analytical and LS-DYNA density and pressure distribution along the 1D plane strain domain. For the purposes of this illustration the artificial bulk viscosity coefficient have been doubled from their default values, i.e. $Q_1 = 3.0$ and $Q_2 = 0.12$ and the 0.01 mesh spacing is used.

The shaded area in the density plot, up to a distance of about 0.18, Noh refers to as "error in density due to the type 1 wall heating error." The heating arises from the error in predicting the internal energy. The density in the shocked region is given by $\rho^+ = 2P^+ / 3\varepsilon^+$ and the pressure $P^+ = 4/3$ is correct in this region, see right image in Figure 4. So too much internal energy causes an under prediction of the density and conversely, too little internal energy causes an over prediction of the density. Beyond this region, i.e. R>0.18, the pressure does not agree with the analytical solution. Between the tracer particles located at 0.175 and 0.225, or a distance of 0.05 or 5 elements, the shock pressure is 'smeared' over these elements by the viscosity.

[1] This two material restriction has subsequently been removed.

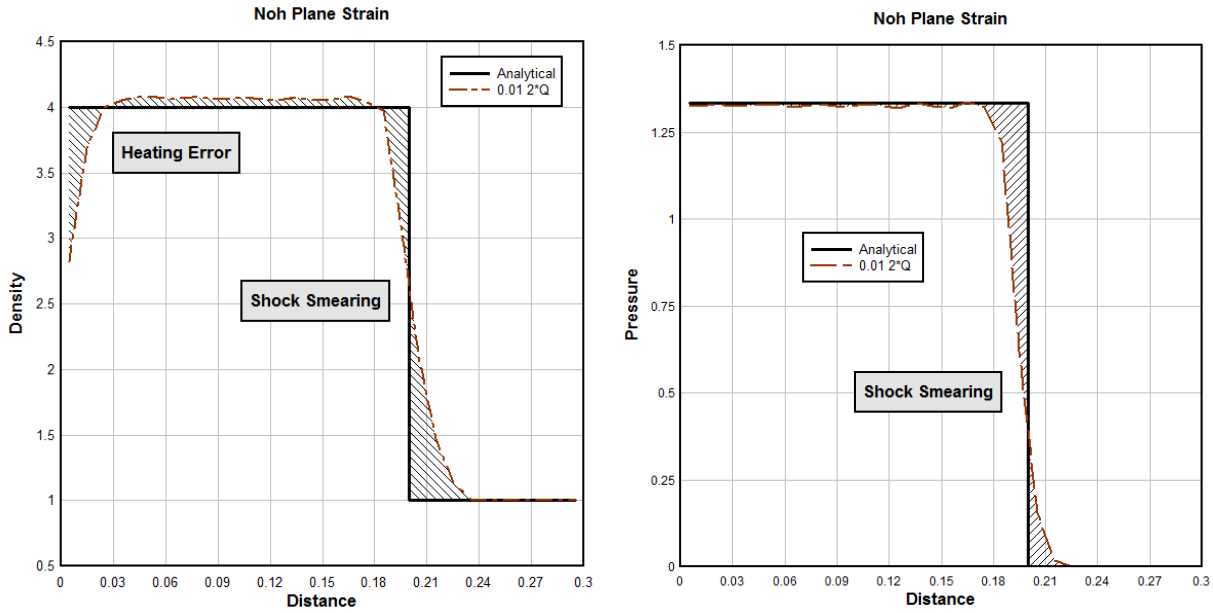

Figure 4 Comparison of analytical and LS-DYNA density (left) and pressure (right) distributions at t=0.6.

Changing the Artificial Bulk Viscosity Coefficient Values

To illustrate the effect of changing (reducing) the artificial bulk viscosity coefficients, the above describe simulation was repeated with the default LS-DYNA bulk viscosity coefficients, i.e. $Q_1 = 1.5$ and $Q_2 = 0.06$, and compared with the previous results, as shown in Figure 5. The cross hatched region in the density plot (left image) shows a reduction in the wall heating error near the origin, then an increased error to a range of about R=0.15. The shock smearing pressure (right image) occurs over a wider region for the reduced artificial bulk viscosity coefficients.

Some of this additional density error is due to the pressures (right image) in this region (0.015<R<0.16) not agreeing as closely with the analytical solution as was the case for the doubled bulk viscosity coefficients. As Noh notes:

> "In particular, a noisier shock results from the use of a smaller [coefficients], but this noise does not seem, in practice, to result in any numerical error."

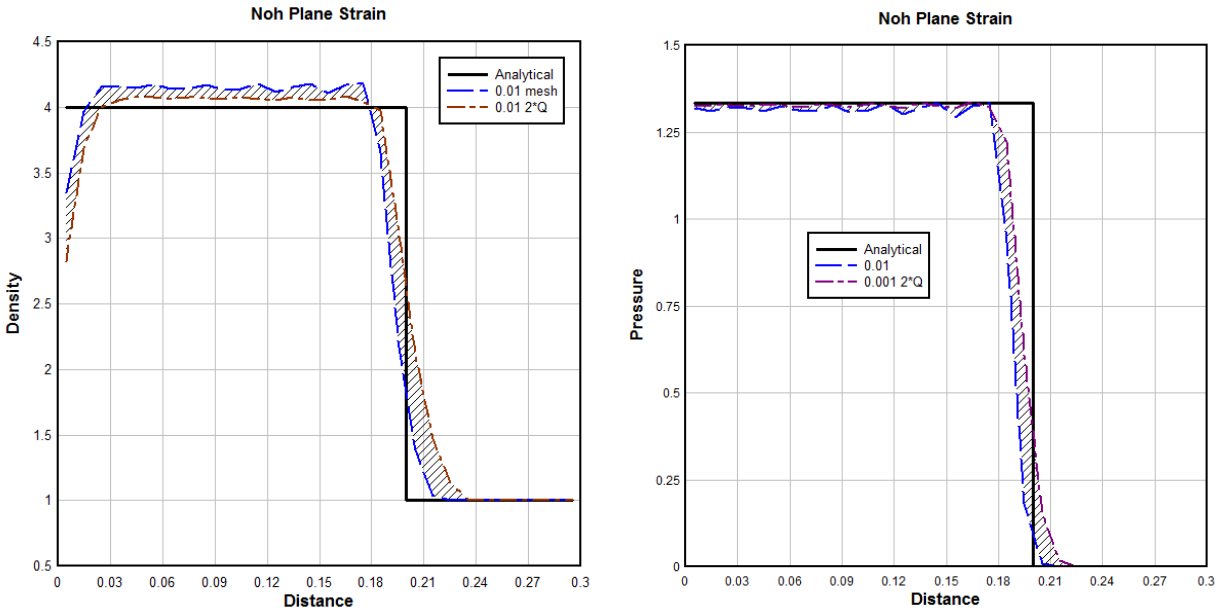

Figure 5 Effect of changing the bulk viscosity coefficients on the computed density (left) and pressure (right) distributions at t=0.6.

Mesh Refinement and Time Step Size

Figure 6 compares the density and pressure distributions for two mesh refinements of 0.005 and 0.01 using the default LS-DYNA bulk viscosity coefficients, i.e. $Q_1 = 1.5$ and $Q_2 = 0.06$. The density distribution indicates a reduction in wall heating error near the origin for the more refined 0.005 mesh and reduced shock smearing region (right image) compared to the coarser 0.01 mesh results.

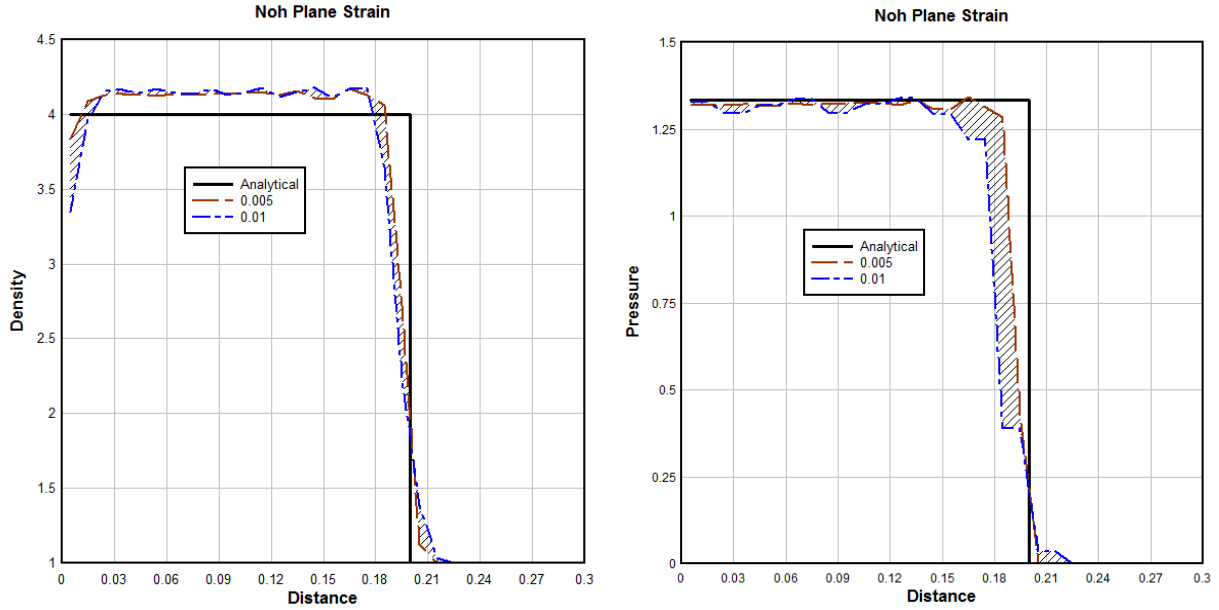

Figure 6 Mesh refinement comparisons of density and pressure distributions for the plane strain geometry.

The LS-DYNA selected time step for the coarser 0.01 mesh spacing was initially 0.002, but switched to a 50% larger time step size of 0.003 by cycle 9 and then remained constant. This time step size is a bit surprising as something on the order of the element length divided by the shock speed, i.e. $0.01/(1/3)=0.03$ might be expected. Noh's benchmark problem provides an opportunity to highlight the role of the artificial bulk viscosity in LS-DYNA's time step selection. A discussion of initial and subsequent time step size determination by LS-DYNA is provided in an appendix.

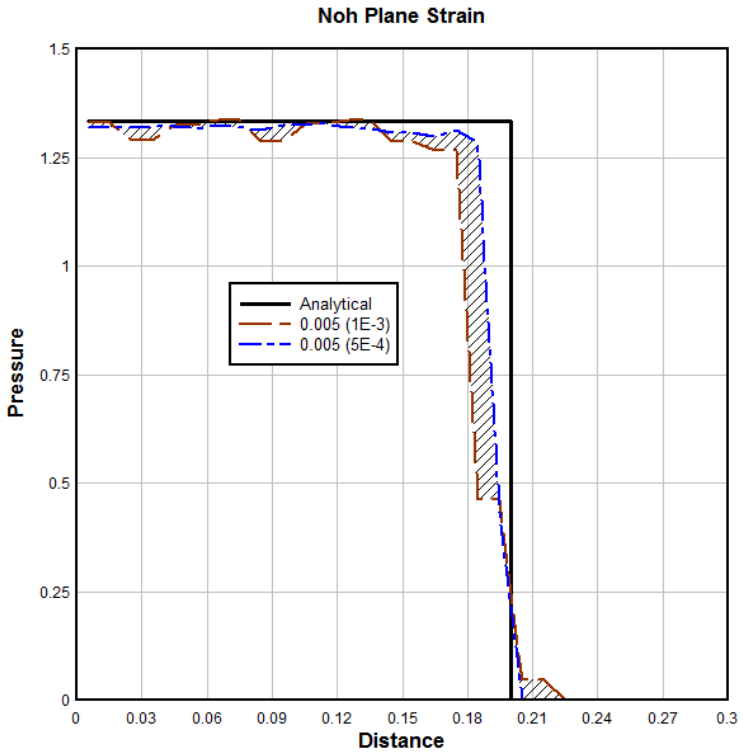

Figure 7 Comparison of pressure distributions at t=0.6 for two different time step sizes.

Three Dimensional Spherical Simulation Results

For completeness, the results for the two dimensional axisymmetric geometry are included in an appendix. The discussion for the axisymmetric and 3D spherical results are quite similar, but the 3D spherical case merits the reader's attention as this is the most practical of the three geometries. The spherical geometry is used to model the important case of free air burst and used with the LS-DYNA mapping capability to include free air blasts up to the point where structure or boundary interaction occurs.

Figure 8 shows comparisons of the analytical and LS-DYNA density and pressure distributions for the 3D spherical domain. The LS-DYNA default artificial bulk viscosity coefficients have been used, i.e. $Q_1 = 1.5$ and $Q_2 = 0.06$, with the nominal 0.01 mesh spacing used by Noh. The shaded region in each of the two images indicates the error between the analytical solution and the LS-DYNA simulation results. These error regions are much larger than was observed for the 1D plane strain case, i.e. Figure 4, and are not limited to the wall heating error near the origin and shock smearing error.

The significant after shock density error is a combination of the wall heating error and the increasing density due to the convergent ideal gas flow toward the origin. The pressure behind the shock is nearly constant at about 14.2, but under predicts the analytical pressure of 20.3 by 30%. As will be demonstrated, mesh refinement will minimize both this pressure error and the error in the density result.

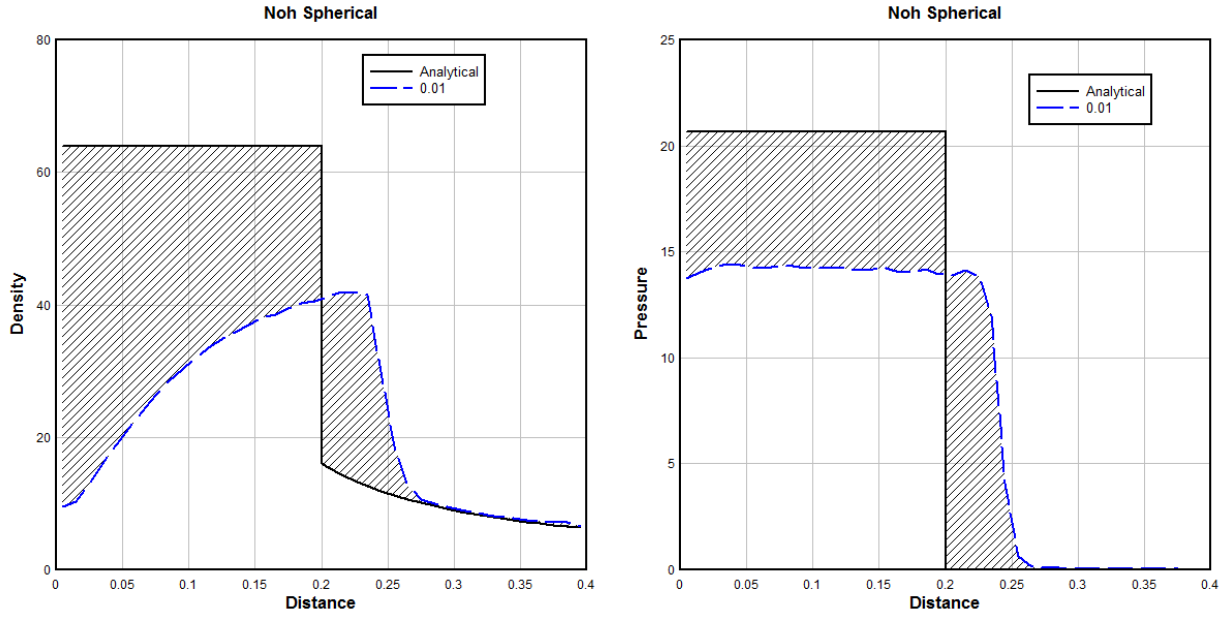

Figure 8 Comparison of analytical and LS-DYNA density (left) and pressure (right) distributions at t=0.6 for Noh's spherical geometry benchmark.

The pressure distribution also shows that the shock smearing does not occur around, i.e. before and after, the analytical shock but occurs at a slightly greater range of about 0.215 rather than the analytical range of 0.2. This shift in the shock smearing region is due once again to the convergent ideal gas flow toward the origin.

Changing the Artificial Bulk Viscosity Coefficient Values

To illustrate the effect of changing the artificial bulk viscosity coefficient, the above described simulation was repeated with decreasing bulk viscosity coefficients, i.e. $Q_1 = 1.0$ and $Q_1 = 0.5$, and compared to the previous default bulk viscosity results in Figure 8. As was noted for the 1D

plane strain simulation results, refer back to Figure 5, the wall heating error in density decreases when the artificial bulk viscosity coefficients decrease. The decreased artificial bulk viscosity coefficients also decrease the error in the pressure behind the shock by increasing the pressure and moving the shock smearing closer to the analytical range of 0.2.

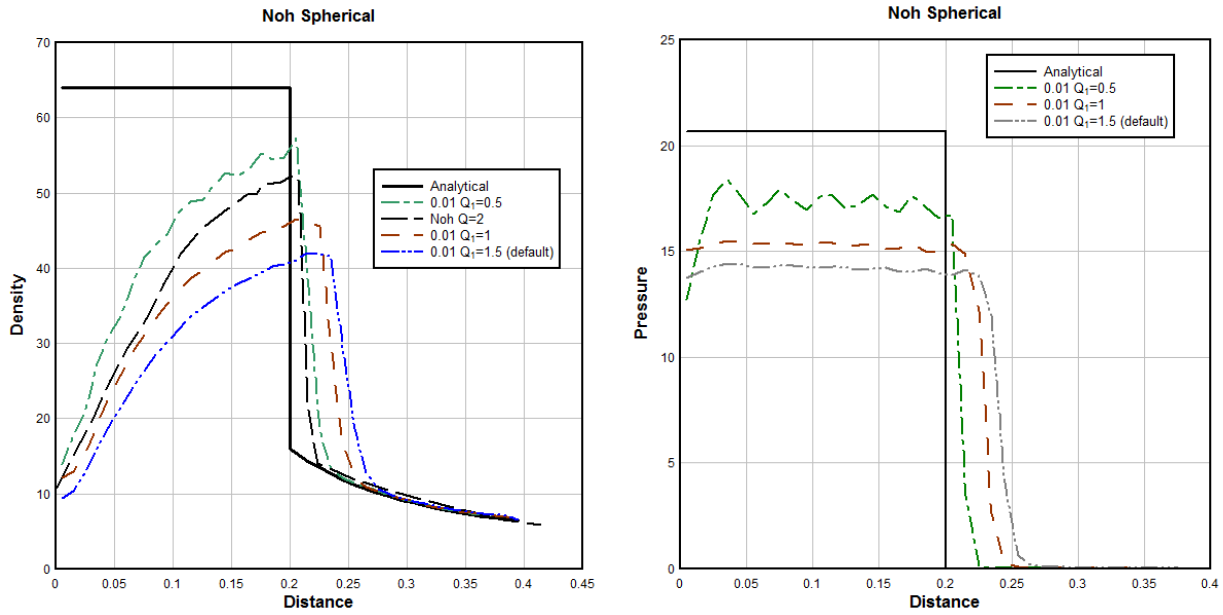

Figure 9 Effect of decreasing the bulk viscosity coefficients on the LS-DYNA spherical simulation density (left) and pressure (right) distributions at t=0.6.

The density distribution shown in Figure 9 (left) includes the benchmark computed result provided by Noh in his Figure 18 using a value of $Q_1 = 2$. It should be noted that using a value of $Q_1 = 2$ with LS-DYNA would provide for *more density error* than is illustrated for the default LS-DYNA case of $Q_1 = 1.5$. The source of this discrepancy between Noh's benchmark result and the LS-DYNA results are not known; a similar discrepancy was noted for Noh's 1D plane strain result provided in his Figure 1.

Mesh Refinement

Figure 9 compares the density and pressure distributions for five mesh refinements varying from a coarse 0.02 to a refined 0.0006 using the default LS-DYNA bulk viscosity coefficients, i.e. $Q_1 = 1.5$ and $Q_2 = 0.06$. The density distribution indicates a reduction in wall heating error near the origin as the mesh is refined and reduced shock smearing width in the pressure distribution. However, neither the density nor pressure distribution is converged, i.e. two mesh refinement producing essentially the same result, even at the finest mesh spacing of 0.006.

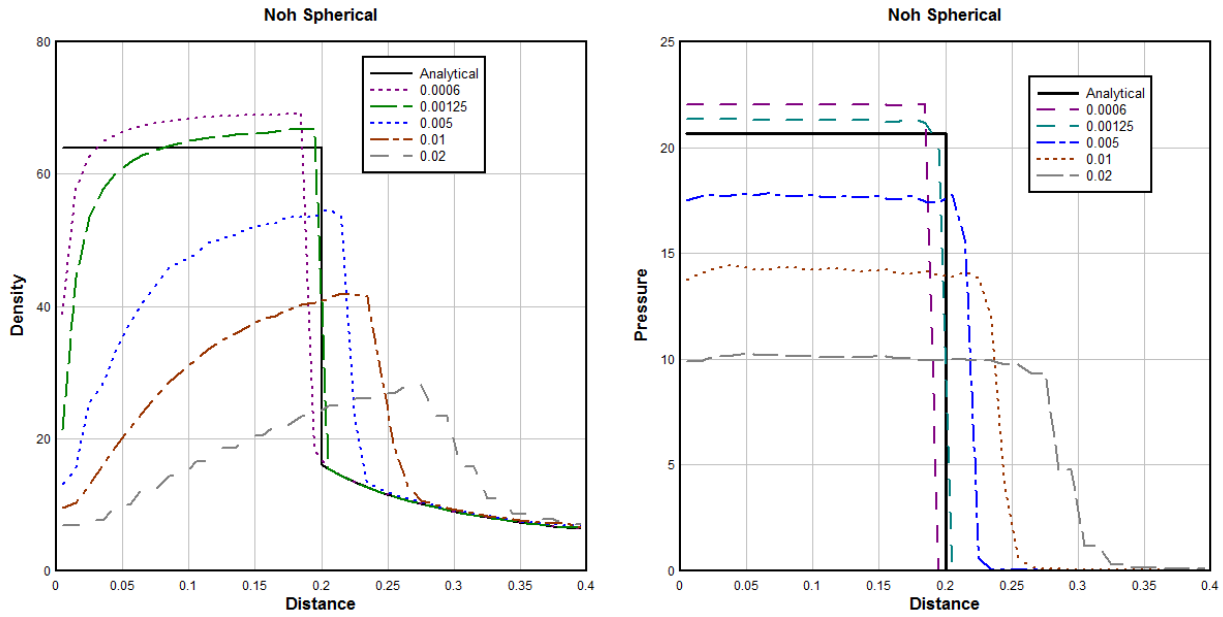

Figure 10 Mesh refinement comparisons of density (left) and pressure (right) distributions for the spherical geometry.

Noh recognizes another form of artificial bulk viscosity error associated with non-uniform meshing[2] – a common practice in large scale 3D blast simulations. Noh uses geometric progression mesh spacing with mesh sizes that decrease from the origin over the first 20 mesh points (nodes) and then increase for the next 20 mesh points. Results are provided for the 1D plane strain case using three difference geometric ratios. Attempts to reproduce Noh results were unsuccessful, as the errors indicated by Noh were much larger than those obtained using LS-DYNA.

While Noh's somewhat odd 1D meshes were useful for his explanation of artificial bulk viscosity errors associated with non-uniform meshing, such meshes are of no practical value to analysts. What is often done in practice is to use geometric progression meshes with increasing element size as a function of distance from the shock source. Such a 1D spherical mesh was constructed using 40 elements between the origin and R=0.2, i.e. location of the shock front a t=0.6. The element nearest the origin had length 0.00125 and the element at the shock front, and those for larger values of the radius, all having uniform lengths of 0.005.

Figure 11 compares the density and pressure distributions for two mesh configurations of uniform 0.005 lengths and a mesh using a geometric ratio of increasing mesh size from the origin. The hatched areas indicate the difference between the uniform and ratio meshes. There is a significant reduction in error when the uniform mesh is used compared to the ratio mesh. Both meshes have 40 elements in the region from origin to R=0.2. But the initial 0.00125 element size in the ratio mesh will make for a smaller time step for the duration of the simulation. This comparison would indicate ratio meshes are to be avoided in favor of uniform meshes.

[2] Section 6 "Q ERRORS FOR A NONUNIFQRM MESH."

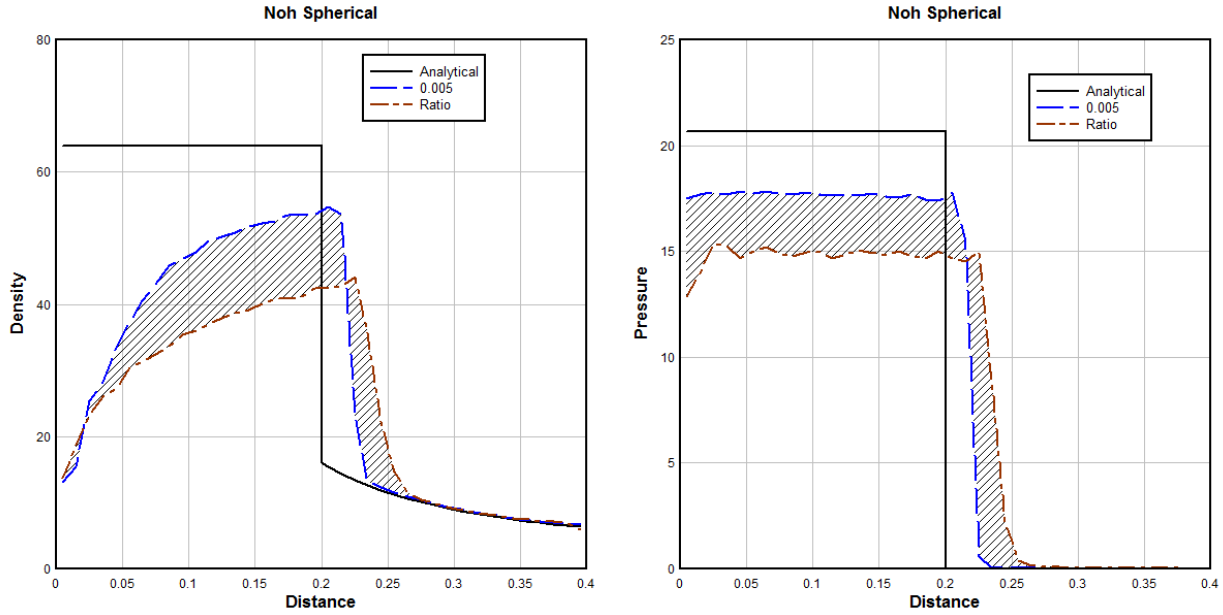

Figure 11 Comparison of density (left) and pressure (right) distributions for a uniform mesh (0.005) and a geometric progression mesh (Ratio).

Practical Application

The analytical solution, and benchmark simulation results, presented by Noh provides a basis for verification of artificial bulk viscosity implementations. However, of necessity a much simplified problem definition is needed to obtain such an analytical solution. Such simplified problems seldom are representative of corresponding more complex practical simulations.

As a specific illustration, consider the enclosed cylinder explosive tests reported by Kuhl et al. (1998). A fully confined explosion using 875g of TNT inside a 16.6 m^3 cylindrical tank (radius: 1.17m and height: 3.87m) filled with air in one case and nitrogen in a repeat test. The purpose of these test was demonstrate the afterburning energy associated with TNT. The chemical composition of TNT does not include sufficient oxygen to release all of its chemical energy potential; typically additional oxygen is provided by the air surrounding. However, in the case of the nitrogen filled cylinder, there is no additional oxygen available, so the released energy is less. The key data reported in these tests was the residual chamber pressure: of about 0.28MPa in air and about 0.085MPa in nitrogen.

The LS-DYNA Multi-Material Arbitrary Lagrange Eulerian solver was used to simulate the closed cylinder and detonation of the 875g of TNT. An axisymmetric model of half the length of the cylinder and charge was constructed using a uniform 2.5mm mesh. The LLNL TNT charge had a radius of 25mm and an overall length of 273.4mm; the 2.5mm mesh spacing provides for 10 elements across the radius of the charge, which is usually considered a minimum number of elements; a uniform 5mm mesh produced a final chamber pressure only 3% different from the 2.5mm mesh pressure.

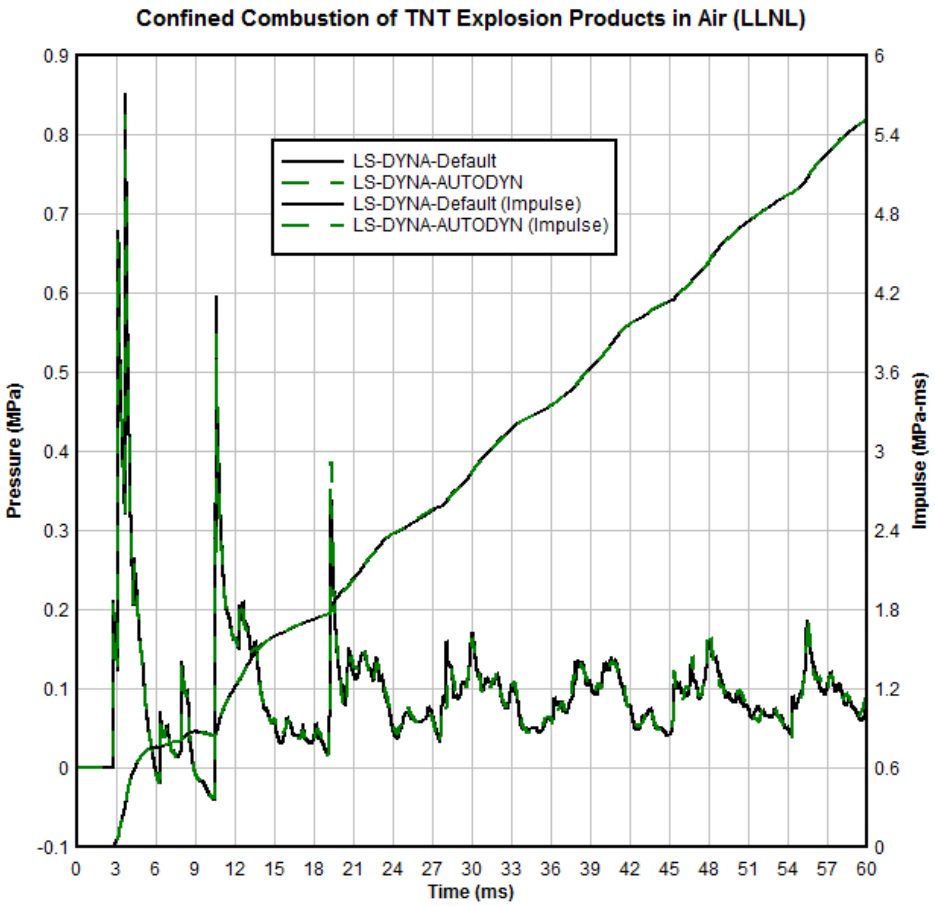

Figure 12 Pressure and impulse for the LLNL closed chamber TNT detonation.

Figure 12 shows the pressure and impulse histories calculated at the top of the cylinder at a radius of 0.585m using the default LS-DYNA bulk viscosity coefficients, i.e. $Q_1 = 1.5$ and $Q_2 = 0.06$, and using the AUTODYN default bulk viscosity coefficients $Q_1 = 1.0$ and $Q_2 = 0.2$. The two results are nearly identical with only some variation in the pressure peaks. The impulse at t=60ms of 5.52MPa-ms can be used to estimate the chamber final pressure by making the simplifying assumption that the pressure is constant over the simulation duration. This final pressure of 0.092MPa (=5.52/60) overestimates by 8% the estimated experimental final pressure of 0.085MPa, determined via a moving average of the measured pressure history. The corresponding impulse-estimated final pressure provided by Edri et al. (2013), using AUTODYN, is 0.109MPa.

For this particular application, changing the artificial bulk viscosity coefficients from the LS-DYNA to the AUTODYN default values does not change the system response of interest, i.e. final cylinder pressure.

Summary

One dimensional LS-DYNA results for plane strain, cylindrical and spherical geometries have been compared with the corresponding analytical solutions of Noh for a shock tube problem. The three types of errors associated with artificial bulk viscosity identified by Noh: (1) excess shock heating, (2) non-uniform meshing and (3) due to spherical geometries, have been demonstrated. For the most part these errors can be minimized via uniform mesh refinement.

In addition to the artificial bulk viscosity errors, an examination of the LS-DYNA minimum time step selection and the roll of the artificial bulk viscosity in the time step calculation is presented in an appendix. Another appendix provides the solution of the Rankine–Hugoniot jump conditions for Noh's problem. The final appendix provides a comparison of Noh's analytical solution with four explicit solvers.

Acknowledgement

The advice, help and especially patient explanations of Dr. Nicolas Aquelet of LSTC in preparing this manuscript are most gratefully acknowledged. The author is most grateful to Dr Yuli Huang for providing the Abaqus and LS-DYNA Lagrange results and Dr. Oliver Siegemund for providing the AUTODYN results.

References

Benson, J.D. (10092) "Computational Methods in Lagrangian and Eulerian Hydrocodes," *Computer Methods in Applied Mechanics and Engineering*, Volume 99 pages 235-394.

Von Neumann, J. and R.D. Richtmyer, (1950) "A Method for the Numerical Calculation of Hydrodynamic Shocks," *Journal of Applied Physics*, Volume 21 (1950).

Landshoff, R. (1955) "A Numerical Method for Treating Fluid Flow in the Presence of Shocks," Los Alamos Scientific Laboratory, LA-1930.

Noh, W.F. (1978) "Errors for Calculations of Strong Shocks Using an Artificial Viscosity and an Artificial Heat Flux," *Journal of Computational Physics*, Volume 72, Pages 78-120.

Sod, G.A. (1978). "A Survey of Several Finite Difference Methods for Systems of Nonlinear Hyperbolic Conservation Laws," *Journal of Computational Physics*, Volume 27, Pages 1–31.

Kuhl A.L, J. Forbes, J. Chaudler, A.K Oppenheim, R. Spektor, and R.E.Ferguson (1998). "Confined combustion of TNT explosion products in air," Lawrence Livermore National Laboratory Report UCRL-JC-131748, Livermore, CA USA.

Edri1,I., V.R. Feldgun, Y.S. Karinski and D.Z. Yankelevsky, (2013), "Afterburning Aspects in an Internal TNT Explosion," *International Journal of Protective Structures*, Volume 4, Number 1, pages 96-116.

Appendix – Two Dimensional Axisymmetric Simulation Results

As mentioned in three dimensional spherical results section, the results for the two dimensional axisymmetric geometry are quite similar to those for the spherical geometry. Thus only the basic density and pressure distribution, using the default LS-DYNA artificial bulk viscosity coefficients and the nominal 0.01 mesh, are presented in this section, see Figure 13.

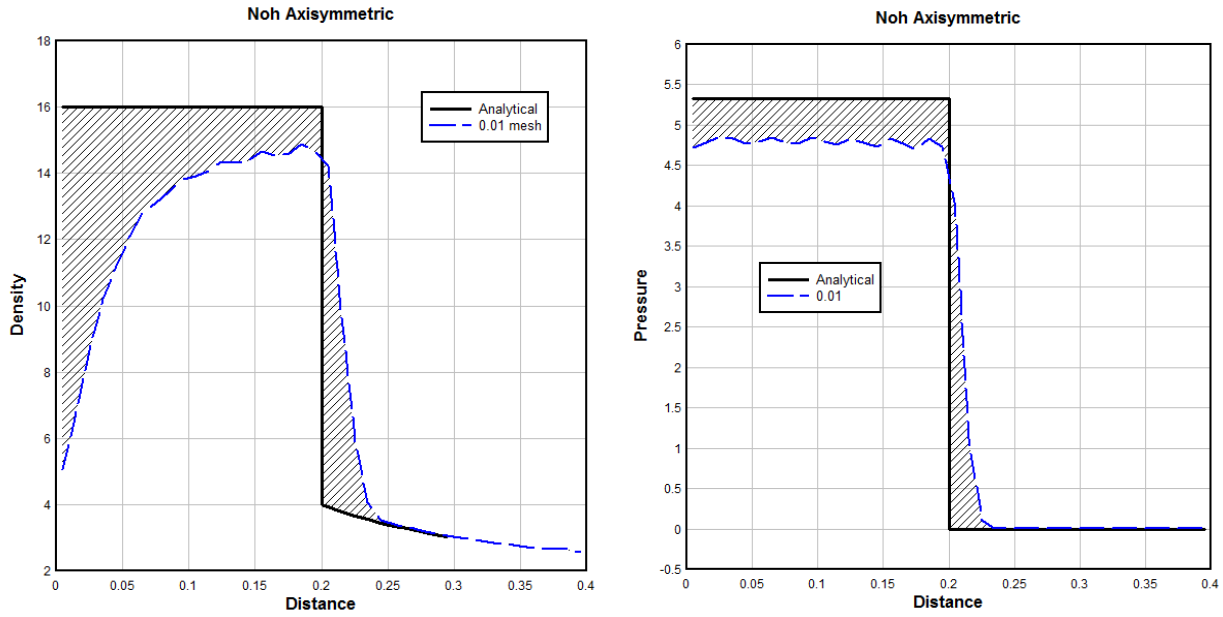

Figure 13 Comparison of analytical and LS-DYNA density (left) and pressure (right) distributions at t=0.6 for Noh's axisymmetric geometry benchmark.

Appendix – Time Step Calculations

Typically one does not think about the artificial bulk viscosity affecting the time step, but this benchmark problem allows an opportunity to highlight the role of the artificial bulk viscosity in LS-DYNA's time step selection. From the LS-DYNA Theoretical Manual Equations 3.2 and 3.3:

$$\Delta t_c = \frac{L_c}{Q + \left(Q^2 + c^2\right)^{1/2}} \tag{3.2}$$

where Q is a function of the bulk viscosity coefficients C_0 and C_1

$$Q = \begin{cases} C_1 c + C_0 L_c \left|\dot{\varepsilon}_{kk}\right| & \text{for } \dot{\varepsilon}_{kk} < 0 \\ 0 & \text{for } \dot{\varepsilon}_{kk} > 0 \end{cases} \tag{3.3}$$

For Noh's problem ahead of the shock the local sound speed c is zero since there is no internal energy and $\dot{\varepsilon}_{kk} = \Delta u / \Delta x = -1/0.01 = -100$ so $Q = Q_1 L_c \left|\dot{\varepsilon}_{kk}\right| = Q_1$ and

$$\Delta t_c = \frac{L_c}{Q + \left(Q^2 + c^2\right)^{1/2}} = \frac{L_c}{2Q} = \frac{0.01}{3} = 3.33 \times 10^{-3} \tag{5}$$

and finally

$$\Delta t = \left(\text{TSSFAC}\right)\Delta t_c = \left(0.6\right)3.33 \times 10^{-3} = 2.0 \times 10^{-3} \tag{6}$$

For the cylindrical geometry

$$\begin{aligned} \dot{\varepsilon}_{kk} &= \frac{u}{r} + \frac{\Delta u}{\Delta r} = \frac{-0.5}{0.005} + \frac{-1}{0.01} = -200 \\ Q &= C_0 \Delta r \left|\dot{\varepsilon}_{kk}\right| = 1.5\left(0.01\right)200 = 3 \\ \Delta t &= \left(\text{TSSFAC}\right)\Delta t_c = \left(\text{TSSFAC}\right)\frac{\Delta r}{2Q} = 0.6\frac{0.01}{6} = 1.0 \times 10^{-3} \end{aligned} \tag{7}$$

For the spherical geometry

$$\begin{aligned} \dot{\varepsilon}_{kk} &= 2\frac{u}{r} + \frac{\Delta u}{\Delta r} = 2\frac{-0.5}{0.005} + \frac{-1}{0.01} = -300 \\ Q &= C_0 \Delta r \left|\dot{\varepsilon}_{kk}\right| = 1.5\left(0.01\right)300 = 4.5 \\ \Delta t &= \left(\text{TSSFAC}\right)\Delta t_c = \left(\text{TSSFAC}\right)\frac{\Delta r}{2Q} = 0.6\frac{0.01}{9} = 6.66 \times 10^{-4} \end{aligned} \tag{8}$$

These three initial time steps for the element nearest the origin agree with the results from the LS-DYNA d3hsp file list of initial time steps.

However, all the other elements in the plane strain and cylindrical geometries have an initial time step of 3×10^{-3}. This time step is computed from the simple relationship:

$$\Delta t_u = \left(\text{TSSFAC}\right)\frac{\Delta x}{2}\frac{1}{|u|} = \left(0.6\right)0.005\left(1\right) = 3\times10^{-3} \tag{9}$$

that provides a time step ensuring the average velocity u in an element does not cause motion of more than half way across the element length Δx. This initial time step and others computed from the Courant condition, e.g. Equation (3.2) above, and contact stability, etc., are assessed by LS-DYNA to determine the minimum applicable time step for each element.

For the plane strain geometry, $\dot{\varepsilon}_{kk} = \Delta u / \Delta x = 0$ since $\Delta u = 0$ for all elements other than the element nearest the origin, Thus the minimum initial time step for all these elements is $\Delta t_u = 3\times10^{-3}$.

For the cylindrical geometry, consider the second element with $\Delta u = 0$, $u = -1$ and $r = 0.015$ then from Equation (7), $\dot{\varepsilon}_{kk} = -1/0.015 = -66.66$ and subsequently $\Delta t = 3\times10^{-3}$ the same value as Δt_u . For the third element with $\Delta u = 0$, $u = -1$ and $r = 0.025$ then $\dot{\varepsilon}_{kk} = -1/0.025 = -40$ and subsequently $\Delta t = 5\times10^{-3}$ is larger than the value of Δt_u , so Δt_u is set as the initial time step. All subsequent elements will have Courant time steps larger than Δt_u.

For the spherical geometry, the second and third elements will have Courant time steps smaller than Δt_u, and all other elements will have larger Courant time steps. Consider the second element with $\Delta u = 0$, $u = -1$ and $r = 0.015$ then from Equation (8), $\dot{\varepsilon}_{kk} = -2/0.015 = -133.33$ and subsequently $\Delta t = 1.5\times10^{-3}$ smaller than Δt_u.

After the initial time step, the element nearest the origin, and subsequently its neighbors, will be compressed thus have internal energy and non-zero wave speed equal to the shock speed $S = 1/3$. From Equation (5) it is observed that the Courant time step for all such compressed elements will be larger than the initial time step, and larger than Δt_u. Thus Δt_u will be used for the remainder of the simulation until all the elements are compressed, which does not occur for the benchmark duration.

Appendix – Rankine–Hugoniot Jump Conditions

The equations and derivation in this section follow the Wikipedia presentation of the Rankine–Hugoniot conditions:

https://en.wikipedia.org/wiki/Rankine%E2%80%93Hugoniot_conditions

The following three conservation equations, mass, momentum and energy, are Equations (12), (13) & (14) in the Wikipedia article.

$$u_s\left(\rho_2 - \rho_1\right) = \rho_2 u_2 - \rho_1 u_1 \tag{10}$$

$$u_s\left(\rho_2 u_2 - \rho_1 u_1\right) = \left(\rho_2 u_2^2 + p_2\right) - \left(\rho_1 u_1^2 + p_1\right) \tag{11}$$

$$u_s\left(\rho_2 E_2 - \rho_1 E_1\right) = \rho_2 u_2\left(e_2 + \frac{u_2^2}{2} + \frac{p_2}{\rho_2}\right) - \rho_1 u_1\left(e_1 + \frac{u_1^2}{2} + \frac{p_1}{\rho_1}\right) \tag{12}$$

Where specific total energy E is given by

$$E = e + \frac{u^2}{2} = \frac{P}{\rho(\gamma - 1)} + \frac{u^2}{2} \tag{13}$$

and use has been made of the equation-of-state $p = (\gamma - 1)\rho e$

For the special case considered by Noh

Post Shock	Pre-Shock
$u_1 = 0$	$u_2 = -1$
$\rho_1 = ?$	$\rho_2 = 1$
$p_1 = ?$	$p_2 = 0$
$e_1 = ?$	$e_0 = 0$
$u_s = ?$	
$\gamma = 5/3.$	

There are four equations, i.e. Equations (10), (11) & (12) and the equation-of-state, and four unknowns: ρ_1, p_1, e_1 and u_s .

Simplifying the above three conservation equations by introducing the known quantities:

$$u_s\left(1 - \rho_1\right) = 1 \tag{14}$$

$$u_s = 1 - p_1 \tag{15}$$

$$u_s\left(\frac{1}{2} - \frac{p_1}{\gamma - 1}\right) = \frac{1}{2} \tag{16}$$

Equations (15) & (16) can be solved for the pressure after the shock

$$p_1 = \frac{\gamma - 1}{2} + 1 = \frac{\gamma + 1}{2} = \frac{4}{3} \tag{17}$$

Equations (14) & (15) can be solved for the density after the shock

$$\rho_1 = 1 - \frac{1}{1-p_1} = \frac{-p_1}{1-p_1} = \frac{-4/3}{-1/3} = 4 \tag{18}$$

Finally, the shock speed is obtained from Equations (15) and (18)

$$u_s = 1 - p_1 = 1 - \frac{4}{3} = \frac{-1}{3} \tag{19}$$

Where the minus sign arises do to the arbitrary selection of which quantities are before and after the shock.

Appendix – Other Explicit Solver Results

Although the shock wave problem posed by Noh is purely academic, it does serve as a verification case study, i.e. comparisons to analytical solutions, and can be used illustrate differences in artificial bulk viscosity implementations. Two collaborators were asked to contribute numerical solutions to Noh's three geometric cases, using default artificial bulk viscosity parameters.

In addition to the LS-DYNA Eulerian results presented in the body of this manuscript, the following results are compared in this appendix:

- LS-DYNA – Lagrange solver with $Q_1 = 1.5$ and $Q_2 = 0.06$
- Abaqus – Lagrange solver with $Q_1 = 1.5$ and $Q_2 = 0.06$
- AUTODYN – Eulerian solver with $Q_1 = 1.0$ and $Q_2 = 0.2$

Typically shock wave problems are solved using Eulerian solvers because, in general, the range of applicability of standard Lagrange solvers for such problem is quite limited due to element distortion. For Noh's problem a Lagrange solver is appropriate, and perhaps that is what Noh also used. Additionally, for a fixed initial mesh, Lagrange solvers are more accurate than Eulerian solvers as the presence of the advection term reduced the order of accuracy.

The collaborator providing the Abaqus results did not feel sufficiently experienced with the Eulerian solver, but (cleverly) noted the Lagrange solver was applicable for these simulations. To provide a basis of comparison, the same Lagrange modeling techniques were used with LS-DYNA. The reader should recall that for the LS-DYNA Eulerian results, the same one dimension mesh of beam elements was used for all three geometries, i.e. plane strain, axisymmetric (cylindrical) and spherical, implemented via an element formation input option. For the Lagrange models, there is no such convenient one dimension element. The Lagrange models used quadrilateral shell elements appropriately arranged and constrained for the geometries. For the plane strain case, a line of plain strain shell elements constrained from lateral motion – 3D solids were also used and provided identical results. For the cylindrical case, the same shell mesh used for the plane strain case was again used, but with the optional element formulation for axisymmetric geometry. The spherical case had a 'pie shaped' arrangement of shell elements and the axisymmetric geometry option completed the model.

The AUTODYN collaborator used essentially the same meshing and constraint method as described above for the Abaqus and LS-DYNA models. One difference in the AUTODYN mesh is the removal of the triangle shaped element that results from the 'pie shaped' mesh at the origin. In standard spherical blast problems, where the explosive is at the origin of the spherical mesh, AUTODYN recommends that the removal of this small portion of the explosive be limited to 1/100 of the charge radius. Interestingly, the Lagrange LS-DYNA and Abaqus results were also run without the apparently troublesome triangular element at the origin. Part of the problem with quadrilaterals that degenerate into triangles is the mass is doubled at one of the four nodes. This causes a mesh dependency if the element nodes are renumbers, and in the case of the LS-DYNA results induced excessive hourglassing.

Plane Strain Results

Figure 14 compares Noh's plane strain analytical solution for pressure (top) and density (bottom) with four explicit solvers. All four pressure distributions closely approximate the analytical solution with the two Lagrange solutions (LS-DYNA & Abaqus) performing better than the two Eulerian solutions. The LS-DYNA Eulerian solution predicts a slower shock speed relative to the other solutions, as the computed shock front is not as far down range as the other results at the time of 0.6.

For the density distributions, again the Lagrange solutions closely approximate the analytical solution. In this case the LS-DYNA Lagrange solution agrees with the analytical solution except for near the origin and exhibits a small amount of shock smearing at the shock front. A similar comparison for the Abaqus solution, although the density after the shock is slightly over predicted. The LS-DYNA Eulerian solution exhibits shock heating near the origin, then over predicts the density behind the shock by about 3% and has significant shock smearing. The AUTODYN solution does not exhibit shock heating at the origin, perhaps due to the missing inner most element so radius 0.01. Unlike the other explicit density results, AUTODYN under predicts the density behind the shock by about 3%, but has less shock smearing then the LS-DYNA Eulerian result.

Recall, that when the pressures agree with the analytical solution, any variation in the density distribution can be thought of as due to the internal energy calculation, since the ideal gas equation of state is $p = (\gamma - 1)\rho e$. Thus the effects of artificial bulk viscosity are evident in the density distributions.

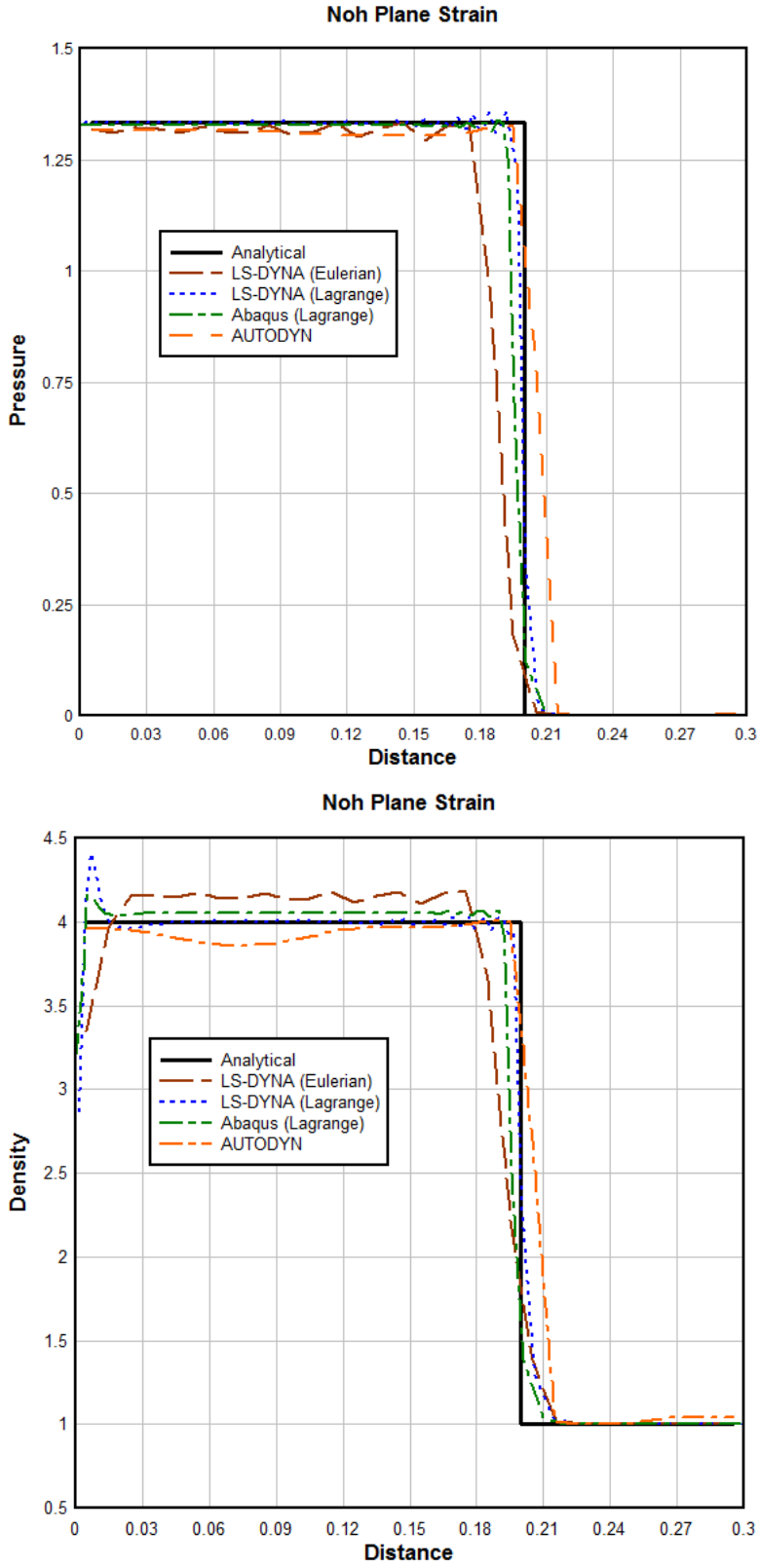

Figure 14 Comparisons of analytical solutions for pressure (top) and density (bottom) for Noh's plane strain geometry with results from four explicit solvers.

Axisymmetric (Cylindrical) Results

Figure 15 compares Noh's axisymmetric (cylindrical) analytical solution for pressure (top) and density (bottom) with four explicit solvers. For this geometry, all four explicit solutions under predict the pressure after the shock with the Abaqus Lagrange results most closely tracking the analytical pressure distribution. The LS-DYNA Lagrange solution under predicts the pressure after shock pressure by about 6%, while the LS-DYNA Eulerian solution under predicts the pressure by about 10%. AUTODYN under predicts the pressure after the shock by about 13%. The Abaqus Lagrange solution also has the least shock smearing of the four pressure results. The LS-DYNA Lagrange solution and AUTODYN solution predict a faster shock speed than the analytical solution as the shock front is farther down range at the time of 0.6.

The two LS-DYNA density distributions, i.e. Eulerian and Lagrange, are nearly identical, despite a noticeable difference in pressure after the shock. This indicates the internal energies for the two solutions must be different since the equation-of-state is $p=(\gamma-1)\rho e$. The two LS-DYNA solutions also exhibit the most shock heating at the origin (rigid wall). The Abaqus Lagrange solution exhibits less shock heating than the LS-DYNA solutions, but also over predicts the density immediately behind the shock. Since the Abaqus pressure was constant behind the shock this implies the internal energy must be less than the analytical value $e=0.5$. Noh refers to this over prediction of the density behind the shock as "Type 2 Error" that he demonstrates using non-uniform (geometrical ratio) mesh sizes. For a Lagrange solution where the mesh size is changing over time, this Type 2 error might be a result – although the LS-DYNA Lagrange solution does not over predict the density behind the shock. Finally, the AUTODYN density distribution shows less shock heating in the vicinity of the wall than the LS-DYNA solutions.

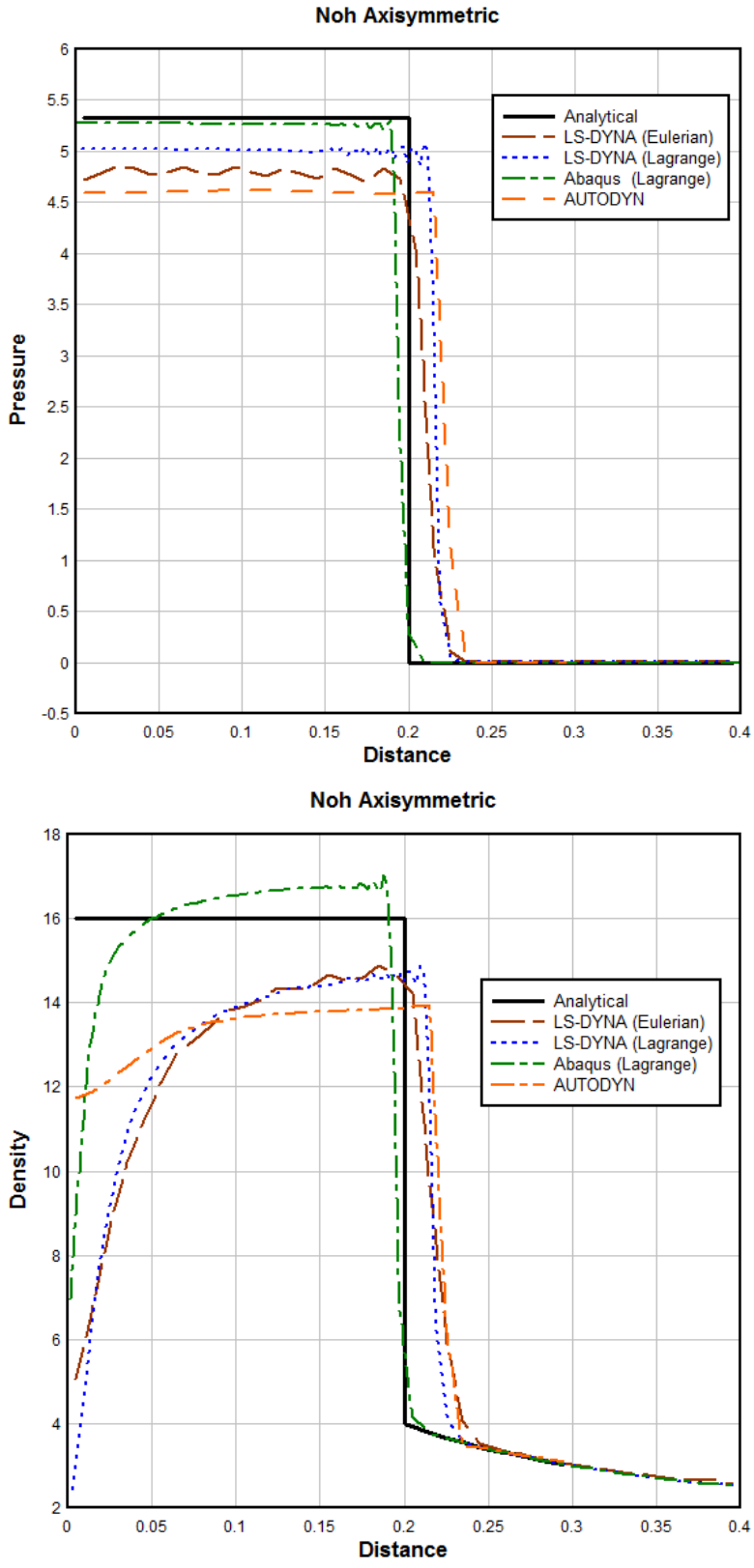

Figure 15 Comparisons of analytical solutions for pressure (top) and density (bottom) for Noh's axisymmetric geometry with results from four explicit solvers.

Spherical Results

Figure 16 compares Noh's spherical analytical solution for pressure (top) and density (bottom) with four explicit solvers. The spherical geometry illustrates the largest difference among the four explicit solutions. The pressure after the shock is over predicted by Abaqus by about 15%, under predicted by LS-DYNA Lagrange by about 9%, under predicted by LS-DYNA Eulerian by about 31%, and AUTODYN under predicts the pressure by 50%. In this geometry, the Abaqus shock speed is slower than the analytical and other three simulations. The AUTODYN pressure ahead of the shock i.e. distances greater than 0.2, exhibits an odd behavior remaining near the same pressure as behind the shock rather than decreasing to the prescribed zero pressure.

The four simulated density distributions have almost nothing in common. Abaqus significantly over predicts the post shock density by about 25%. The two LS-DYNA solutions are quite different, as they were for the pressure distributions. The LS-DYNA Lagrange solution under predicts the density by about 16%, although at least it is nearly a constant density after the shock. The LS-DYNA Eulerian solution exhibits the most shock heat after the passage of the shock front and under predicts the density more than 37%. AUTODYN again provides for an odd response after the shock. The curvature of the density distribution is the reverse of the LS-DYNA Eulerian result and indicates minimal shock heating at the wall. The AUTODYN density does match the analytical solution, $\rho = 16$, at the jump position where the shock wave interacts with the unshocked region with increasing density due to the convergent flow of the spherical geometry. However, the density distribution before the shock arrival does not follow the analytical density distribution, as do the other three numerical results once past thier shock smearing regions.

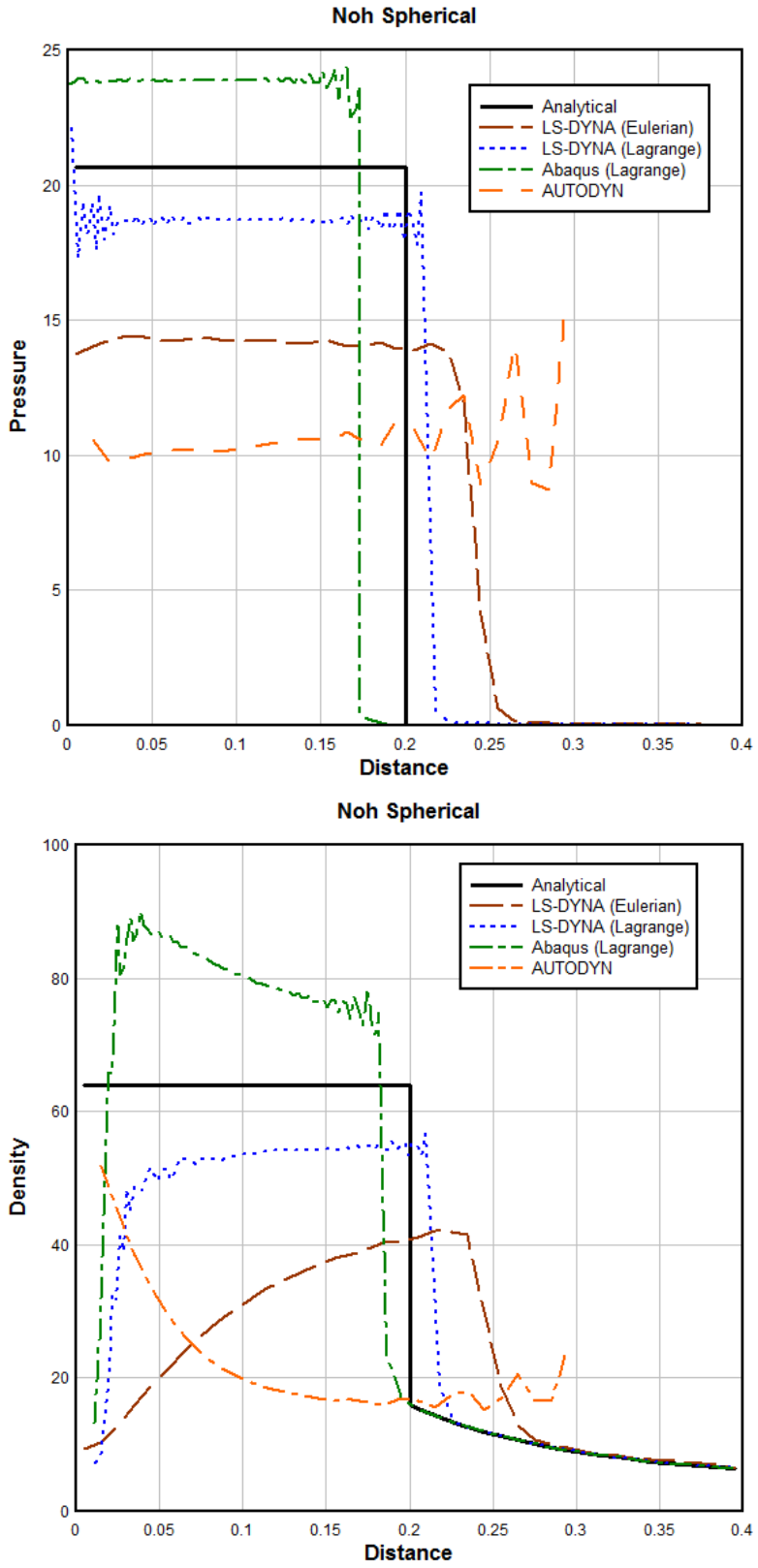

Figure 16 Comparisons of analytical solutions for pressure (top) and density (bottom) for Noh's spherical geometry with results from four explicit solvers.